LAWRENCE
LIVERMORE
NATIONAL
LABORATORY

LLNL-JRNL-666850

Measurement of Carbon Condensation Using Small-angle X-ray Scattering During Detonation of the High Explosive Hexanitrostilbene

M. Bagge-Hansen, L. M. Lauderbach, R. Hodgin, S. Bastea, L. Fried, A. Jones, T. van Buuren, D. Hansen, J. Benterou, C. May, T. Graber, B. J. Jensen, J. Ilavsky, T. M. Willey

February 4, 2015

Journal of Applied Physics

Disclaimer

Measurement of carbon condensates using small-angle x-ray scattering during detonation of the high explosive hexanitrostilbene

M. Bagge-Hansen,[1] L. Lauderbach,[1] R. Hodgin,[1] S. Bastea[1], L. Fried[1], A. Jones,[1] T. van Buuren,[1] D. Hansen,[1] J. Benterou,[1] C. May,[1] T. Graber,[2] B. J. Jensen,[3] J. Ilavsky[4], and T. M. Willey[1,a)]

[1]*Lawrence Livermore National Laboratory, Livermore, CA 94550, USA*
[2]*Washington State University, Pullman, WA, 99164, USA*
[3]*Los Alamos National Laboratory, Los Alamos, NM, 87545, USA*
[4]*Argonne National Laboratory, Argonne, IL, 60439, USA*

The dynamics of carbon condensation in detonating high explosives remains controversial. Detonation model validation requires data for processes occurring at nanometer length scales on time scales ranging from nanoseconds to microseconds. A new detonation endstation has been commissioned to acquire and provide time-resolved small-angle x-ray scattering (SAXS) from detonating explosives. Hexanitrostilbene (HNS) was selected as the first to investigate due to its ease of initiation using exploding foils and flyers, vacuum compatibility, high thermal stability, and stoichiometric carbon abundance that produces high carbon condensate yields. The SAXS data during detonation, collected with 300 ns time resolution, provide unprecedented signal fidelity over a broad q-range. This fidelity permits the first analysis of both the Guinier and Porod / power-law regions of the scattering profile during detonation which contain information about the size and morphology of the resultant carbon condensate nanoparticles. To bolster confidence in these data, the scattering angle and intensity were additionally cross-referenced with a separate, highly calibrated USAXS/SAXS beamline. The data show that HNS produces carbon particles with a radius of gyration of 2.7 nm in less than 400 ns after the detonation front has passed, and this size and morphology are constant over the next several microseconds. These data directly contradict previous pioneering work on RDX/TNT mixtures and TATB, where observations indicate significant particle growth (50% or more) continues over several microseconds. The power-law slope is about -3, which is consistent with a complex disordered, irregular, or folded sp^2 sub-arrangement within a relatively monodisperse structure possessing radius of gyration of 2.7 nm after the detonation of HNS.

I. INTRODUCTION:

High explosives are a compelling system of study for both applied and basic sciences. These fields converge on the central problem of modeling and predicting the explosive energy release behavior of detonating high explosives under practical conditions and without empirical refinement. While certainly the topic of intense research for decades[1-6], the problem persists, in part, due to insufficient experimental resolution for the rapid and complex physical and chemical phenomena occurring during and immediately after (0-1000 ns) detonation. In addition to sub-microsecond timescales, experiments are encumbered by the technical challenges posed by highly exothermic conditions generated by shock-induced compression and heating (P~40GPa, T~4000K) leading to detonation. Significant progress has

a) Author to whom correspondence should be addressed. Electronic mail: willey1@llnl.gov.

been made in developing robust thermochemical models to predict the evolution of the explosive from its solid state (with known elemental composition, density and heat of formation) through: (1) chemical equilibrium of stable products at the so-called Chapman-Jouguet (CJ) state, (2) adiabatic expansion, and (3) afterburn[1, 3, 6]. For a number of technologically important high explosives containing carbon, hydrogen, nitrogen, oxygen (CHNO HEs), current thermochemical models inadequately describe the chemical reaction pathways such that detonation products can be confidently predicted. In particular, the structural and chemical evolution of carbon is vibrantly controversial[7-12]. During denotation, carbon released from highly exothermic decomposition of the solid may undergo a series of gas-phase reactions to produce stable molecular species such as CO and CO_2; however, many common CHNO HEs, e.g., TNT, RDX/TATB mixtures, and HNS) are oxygen deficient, suggesting an alternative fate for excess carbon. Indeed, much more complex, solid carbon aggregates are known to form—an observation leveraged for the industrial production of nano-diamond.[13-15] The presence of such carbon condensation reactions strongly influences detonation models, yet the prevalence, structure, chemistry, and evolution of carbon condensates are expected to vary dramatically, with sensitivity to the source HE. As such, a universal description of carbon condensation reactions and kinetics has proven elusive, despite its acute need in predicting explosive energy release behavior. The significance and complexity of these chemical processes mandate acquisition of experimental input. Here, we describe time-resolved small-angle x-ray scattering (SAXS) experiments, for the first time with sufficient fidelity, to determine carbon condensation kinetics within and immediately behind the hydrodynamic reaction zone of detonating hexanitrostilbene (HNS) from complementary analysis of both the Guinier and Porod / power law regions of the scattering intensity. Our results affirm that SAXS offers a compelling experimental approach to observe carbon condensation kinetics (as suggested by, *e.g.*, Aleshaev *et al.*[16-20]) in CHNO high explosives—an approach that is now rapidly evolving with recent instrumentation developments in synchrotron science that enable adequate statistics (over a suitable q-range) with nanosecond acquisition times.

The relevant timescales considered for condensed phase detonation physics are typically ~1 ns to ~10 μs. In this temporal regime, high explosives display significant diversity in their detonation kinetics as the shock front interacts with materials of different composition and density. The shock front typically propagates through solid CHNO high explosives at speeds of several km-s^{-1}. Denotation proceeds through rapid (~ps) equilibration of molecular translational energy with *inter*- (and then *intra*-) molecular vibrational and rotational modes, leading directly to endothermic bond breaking.[6] Subsequent reactions of ionic and neutral species proceed towards chemical equilibrium at the CJ point on the nanosecond timescale.[1, 2, 4] Diffusion-limited growth of solid and liquid carbon clusters, up to a few nanometers, is also believed to occur under these very high temperature and pressure conditions. The phase of carbon

clusters under these extreme conditions cannot be simply inferred from the bulk carbon phase diagram as their nanometer scale (and thus much larger ratio of surface/bulk atoms) provides an enhanced role to the surface free energy in determining the equilibrium phase [7-11, 14, 21] Beyond the CJ point, the adiabatic expansion of detonation products over microseconds leads to cooling—thus limiting further probable chemical processes. Solid carbon chemistry in this regime may include additional nucleation and growth through gas-solid surface interactions, phase transformation (typically from diamond to graphite), and coagulation/aggregation. These relatively slow processes could be observed over ~10^2-10^4 ns.

For this work, hexanitrostilbene (1,3,5-Trinitro-2-[2-(2,4,6-trinitrophenyl)ethenyl]benzene) was chosen as the first explosive to measure SAXS during detonation at a new beamline and end-station. HNS has high thermal stability, is vacuum compatible, and is reliably initiated with EFIs / slapper initiators[22]. The oxygen deficiency (or, inversely, carbon abundance) of HNS produces copious soot and thus we anticipated a commensurately large SAXS signal intensity. HNS produces sp^2 carbon condensates as opposed to many other explosives, particularly RDX/TNT mixtures, that additionally produce sp^3 or nanodiamond condensates[13-15].

II. EXPERIMENT:

Cylinders of HNS IV high explosives were fabricated at the High Explosives Applications Facility at Lawrence Livermore National Laboratory. HNS IV powders, 400 mg, were uniaxially pressed to 6.34 mm diameter and lengths from 8.13 to 8.36 mm tall with densities ranging from 1.53 to 1.56 g/cm^{-3}. Samples were assigned unique designations and tracked individually from production to detonation so that sample-to-sample variation, particularly density and cylinder height could be considered in subsequent data analysis. **Figure 1** presents details of the experimental setup. Samples were fixed on top of an EFI with a spring-loaded piezo timing pin (Dynasen) at the top of the sample. The assembly was attached to a two-axis motion stage and installed within a ~120 L steel vacuum tank (Teledyne RISI) mechanically designed to fully contain up to 10 g detonations; see **Fig 1 a)**. The tank was modified with entrance and exit windows, see **Fig. 1 b)**, to minimize x-ray attenuation and extraneous scattering during SAXS experiments. X-rays transmit into and out of the chamber through Kapton™ polyimide, poly (4,4'-oxydiphenylene-pyromellitimide, sealed ports (~.125 mm thick). Lexan™ (polycarbonate) panels ranging from .125 to .5 mm were further employed as blast/shrapnel shields in the beam path, and are placed about 200 mm from the sample on the interior of the chamber on both upstream and downstream beam paths. Typically base pressures were <200 mTorr just prior to detonation when all valves to evacuation pumps are closed. The pressure rises to a several Torr after detonation in the sealed vacuum chamber.

Detonation of HNS IV high explosives was shock-induced using an exploding foil initiator (EFI). Early and late estimates for EFI bursts based on the recorded current trace were used as gross estimates

for the initial time the detonation front began to propagate from the bottom of the HNS pellet; see **Figure 1, c)** and **d)**. Correspondingly, the piezo pin, spring-loaded at the top of the HNS cylinder, was used to measure the arrival of the detonation front. Detonation velocities of about 6.3 +/- 0.4 km/s were then calculated using the cylinder height for each individual pellet. These detonation velocities were then employed to estimate the time that the detonation front arrived at the X-ray beam elevation on each sample (fixed at 6.35 mm from the bottom of the HNS cylinders). The corresponding error is ~20 ns based on a gross estimate of initiation of the detonation, and an additional 10-20 ns based on ~100 micron variation in sample alignment in the X-ray beam. In the following results and discussion, all data are temporally calibrated such that t=0 ns is the estimated time (t) that the detonation front reached the X-ray beam center position, computed for every shot individually. The temporal center of the 250 ns camera gate is the designated time for each SAXS trace.

Time-resolved SAXS experiments were performed as part of commissioning operations at the Dynamic Compression Sector (DCS) at the Advanced Photon Source (Argonne National Laboratory) within the special purpose hutch (35-ID-B). This insertion device beamline offers very high flux to a suite of state-of-the-art platforms for materials science under extreme conditions (e.g., shock physics[23, 24]). Focused pink beam, operating in 324-bunch mode, was selected for these experiments with a nominal energy of 23.6 keV (~600 eV fwhm) and spot size of approximately 200 μm x 50 μm, and pulse periodicity of 11.4 ns, and a nominal pulse fwhm of 52 ps. The sample-detector distance was 1.0 m.

Scattering intensity was recorded using an array of four identical area detectors (PI-MAX4 ICCD, Princeton Instruments) focused on the output of a scintillator and image intensifier as described elsewhere[23, 24]. These detectors are capable of sub-nanosecond gating; however, in these experiments, gating was from 50-500 ns (data presented here was acquired with 250 ns gating) in order to capture sufficient numbers of x-ray pulses in the 324 bunch mode. These cameras were focused on the output of an image intensifier (Photek MCP140); care was taken to adjust the image intensifier to avoid saturation, particularly in high-intensity, low-q regions of the images. For this beamline, endstation, and scintillator configuration, 2.5 (on a scale of 5) gave linear response over the intensities measured as outlined in the results section. The scintillator consisting of ~150 μm powdered Lu_2SiO_5:Ce (LSO:Ce) coated on a fiber-optic faceplate. The LSO:Ce has about 50 ns decay time, so each camera frame integrates over the gate time as well as intensity from several x-ray pulses prior to camera gating that persist on the scintillator. Thus, for this particular experiment, the uncertainty in arrival time of the detonation front at the beam position is much less than the integrated time on the camera. The detectors can be configured to trigger in series and are further synchronized with the arrival of x-ray pulses and/or initiation of detonation. **Figure 1 c)** provides a schematic of the relative timing of camera acquisitions with the EFI burst (*i.e.,* initiation of detonation at the bottom of the HNS pellet). A complete and continuous chronology was assembled,

from 0.59 μs before to 3.16 μs after the detonation front passes x-ray beam spot, by interleaving 4-camera acquisitions (cameras designated: C1-C4, each with a gate width of 250 ns) over a series of nominally identical HNS detonations (hereafter, shots HNS-a – HNS-d). **Figure 1** illustrates this scheme for the first two cameras (C1 and C2).

The two-dimensional camera intensity images were reduced to one-dimensional SAXS patterns using the Nika[25] package for the four cameras independently. Scattering angles were calibrated in Nika using silver behenate as scattering angle calibrant. Small-angle scattering data were then reduced, intensity calibrated, and analyzed using the Irena[26] package.

III. RESULTS:

Key metrics for interpreting small-angle x-ray scattering data (especially during commissioning of a new apparatus) are the ability to calibrate both intensity and scattering angles of the instrument to well-known, reliable standards. **Figure 2** presents SAXS from a robust glassy carbon standard[27] previously acquired on 15-ID-D at the APS[28-30] compared with SAXS traces from the 4-camera array used in these experiments; each camera was gated at 250 ns and all other beamline parameters were the same as during the subsequent detonation experiments. The good agreement between these data clearly indicates that we acquired reasonably high quality SAXS from the 4-camera system in the $4x10^{-2}$ to $4x10^{-1}$ $Å^{-1}$ range using this geometry at these particular x-ray energies and intensities. Glassy carbon SAXS was periodically acquired throughout detonation experiments to ensure aligned q-range and calibrated intensities in the subsequent data analysis. To further ensure reasonable linearity in intensity, SAXS data from undetonated HNS was compared to previous USAXS data (**Fig. 3**). This comparison confirms that the normalized SAXS data are well calibrated, and further corroborates confidence in the q-range between ~$4x10^{-2}$ $Å^{-1}$ and $4x10^{-1}$ $Å^{-1}$ in the current SAXS data. The glassy carbon and undetonated HNS SAXS traces acquired on the 4-camera system, in comparison with absolute intensity calibrated USAXS, were used to generate constants for each camera to intensity calibrate the detonation data[26].

The timing configuration in these experiments (**Fig. 1 c**) was set such that camera acquisition windows be interleaved over four separate shots (HNS-a through HNS-d) to provide an uninterrupted chronological sequence and to ensure data reproducibility both shot-to-shot, and camera-to-camera. **Figure 4** shows the corresponding SAXS traces during the early time (-0.59 to 1.16 μs) from cameras C1 and C2. **Figure 5** presents the sequential late time (1.41 to 3.16 μs) SAXS traces from cameras C3 and C4.

As expected, prior to the arrival of the detonation front at the x-ray spot, even after detonation has been initiated, SAXS traces overlay those acquired on HNS prior to detonation; see traces in Fig. 4 at -0.59, -0.35, and -0.08 μs. In contrast, all traces at 0.41 μs through several μs exhibit a distinct SAXS profile with apparently increasing intensity from 0.41 through 1.41 μs traces, and decreasing SAXS

intensity thereafter. One trace, acquired about 0.16 μs after the detonation front passed, appears different from the pre- and post- detonation shots; however, this trace can also be reproduced as a linear-combination fit of pre- and post- detonation SAXS traces.

IV. DISCUSSION:

The time-resolved SAXS data capture a chronological sequence of HNS detonation dynamics. Three temporal regions of interest emerge. First, several SAXS traces (**Fig. 4**) were captured at $t<0$, before the detonation front has passed through the X-ray beam, but after detonation had been initiated by the EFI at the bottom of the sample. These data are consistent with SAXS from undetonated HNS on this instrument as well as data collected on the highly calibrated USAXS instrument at APS[28-30]. Particularly, a power law slope of -4 is observed to the smallest detectable q-range and is consistent with micron-scale voids and porosity observed in undetonated HNS. The second region of interest is immediately after the detonation front. This transitional region is illustrated only by the data at 0.16 μs (**Fig. 4**). By 0.41 μs, the data is representative of late time behavior, dominated by carbon soot condensates—the third region of interest. Further analysis of the transitional data at 0.16 μs reveals that the trace shape *and* intensity can be well reproduced through a simple linear combination of the pre-detonation and late-time SAXS (*i.e.,* regions one and three).

The late time behavior is however remarkable for a number of reasons. First, the SAXS trace shape is essentially unchanged from 0.41 μs to 3.16 μs. To quantify how little the SAXS shape changes, these traces were fit using the unified model with a single Guinier and Porod region[26, 31]. A representative fit is presented in **Figure 6**. The unified fits across shots from 0.41 to 3.16 μs show a power law slope, between 0.1 and 0.2 $Å^{-1}$, of -3.0 +/- .1, and a radius of gyration (R_g) of 27.5 +/- 0.6 Å. **Figure 7** depicts the nearly constant and unchanging radii of gyration extracted from each fit. Thus, post-detonation carbon condensates arrive at their equilibrium size (~2.7 nm R_g) rapidly; indeed, carbon particle growth appears to cease in under 0.4 μs; the first purely late-time SAXS trace. This rapid cessation of particle growth in small-scale HNS detonations is particularly contrary to previous scattering results from TNT/RDX, TATB, and other explosives where measured particulates grow by 50% or more over the first few microseconds after detonation[32].

We hypothesize HNS carbon condensation behavior arises due to one or more of the following possibilities: A large variation in carbon condensate kinetics have been observed using different explosives; HNS might simply perform uniquely with a very rapid initial carbon condensation process followed by no particulate growth over subsequent microseconds. Next, the samples used in this particular experiment are 400 mg and pressure release occurs rapidly at these smaller sizes, potentially

limiting timescales for carbon condensate growth. Finally, this new beamline and its instrumental capability are able to resolve the Guinier region and determine R_g more accurately and with much higher fidelity than previously possible. Experiments are now underway on TNT/RDX mixtures in an attempt to reproduce previous results[32].

An example of the high fidelity is the ability to now obtain data with clear Guinier and associated power law slope at sub-microsecond timescales during and after detonation. HNS carbon condensate small-angle scattering has a -3 slope in the log-log plot between 0.1 and 0.2 $Å^{-1}$. This slope is non-trivial to interpret. One would expect a -4 slope for three-dimensional, nearly monodisperse, spherical particles with smooth and abrupt surfaces, while one might expect close to -2 for disk-like or -1 for rod-like particles.[33-35] Alternatively, the power-law slope can be interpreted in terms of a mass or surface fractal; one might expect a power law slope between -1 and -3 for a mass fractal, or between -2 and -3 for a surface fractal; -3 is an extreme boundary condition under either approximation representing a high volume filling surface or volume fractal morphology. Finally, a broad size distribution of nearly 3D particles could result in scattering observed for the carbon condensates. The SAXS data alone cannot conclusively point to any of the situations above; however, the SAXS pattern is not inconsistent with reasonably monodispersed morphology with radius of gyration ~ 3 nm sp^2 carbon, whether particles with a very high degree of volume and/or surface disorder, or some other more complex structure, i.e. sp_2 carbon nanoribbons that have been observed in detonation soots[15].

Although Guinier and Porod regions return constant Rg's and power laws in the presented traces acquired from 0.41 μs to 3.16 us, the intensity of the scattering does vary with time. The calibrated (*vide supra*) scattering intensity is observed to increase monotonically from 0.41 μs to 1.41 μs then decrease over the very late time regime from 1.41 μs to 3.16 μs (**Figs. 4, 5**). At first glance one might assume this suggests the number of carbon condensate particles is initially increasing from 0.41 to 1.41 us, but if this was the case, one might expect sizes and shapes of particles to change when formed at different times during this very dynamic pressure and temperature environment. Particles are forming between 0 and 0.41 μs as seen in the dramatic changes to scattering from pre- to post-detonation and illustrated by the transition trace at 0.16 μs. We postulate the intensity-only changes at times later than 0.41 μs likely arise from a complex interplay between scattering contrast and the number of particles along the x-ray path. Initially, within the reaction zone, the background gas density is approximately that of the full density undetonated explosive and thus provides very little contrast to carbon condensates. As the gasses and condensates expand outwards, the scattering contrast for particles increases as the density of the background gasses decrease, but the number of carbon particles within the probe beam volume also decreases.

This hypothesis that the SAXS intensity changes due to a temporal scattering contrast effect rather than additional particle production was tested by combining estimates of gas density and radial expansion using ALE3D to compute a gross estimate for the scattering contrast, and then using the experimental data to estimate volume fraction of the carbon condensates. The crude estimate of average gas density and radial expansion was used as a background against full-density graphite to estimate scattering contrast. These led to estimates of volume fractions of 4.4% at 0.66 μs generally monotonically decreasing to 3.3% at 2.11 us. The crude approximations do likely underestimate the volume fraction as the computation estimates 13.4% mass fraction of excess carbon, but the monotonic decrease provides evidence that scattering contrast plays a large, if not dominant role in the varying intensity at microsecond timescales.

The data indicate carbon condensates from detonating HNS form very rapidly, in 0.41 μs or less, after the detonation front passes, and do not continue to evolve in size or shape at later microsecond timescales. This is in direct contradiction to what has been presented previously detonating other materials including TNT/RDX mixtures, TNT, and TATB. The next steps will be to measure the dynamics at timescales much less than hundreds of ns using single, sub-nanosecond x-ray pulses. APS provides an optimal 24-bunch mode, in which ~80 ps fwhm pulses arrive every 153.4 ns; shots can be interleaved temporally to achieve ~10 ns steps in time or better to determine carbon condensate growth kinetics. Such studies have commenced. Experiments are also underway to investigate TNT/RDX mixtures and other explosives to determine both kinetics of formation as well as morphology of carbon condensates.

V. CONCLUSIONS:

New experimental insights into the dynamics of carbon condensation in detonating high explosives are provided through time-resolved SAXS of detonating hexanitrostilbene (HNS). HNS was selected due to its ease of initiation using exploding foils and flyers, vacuum compatibility, high thermal stability, and stoichiometric carbon abundance that produces high carbon condensate yields. SAXS data was collected with 300 ns time resolution and unprecedented signal fidelity over a broad q-range of ~$4x10^{-2}$ $Å^{-1}$ and $4x10^{-1}$ $Å^{-1}$. The scattering angle and intensity were additionally cross-referenced with a separate, highly calibrated ultra-SAXS/SAXS beamline. The SAXS data are of sufficient quality to merit robust analysis of both the Guinier and power-law regions of the scattering profile. The data show that HNS produces carbon particles with a radius of gyration of 2.7 nm in less than 400 ns after the detonation front has passed, and this size is constant over the next several microseconds. The power-law slope is about -3, which is consistent with a disordered, irregular, or folded sp^2 sub-arrangement within a

relatively monodisperse structure possessing radius of gyration of 2.7 nm after the detonation of HNS. These data directly contradict previous pioneering work on RDX/TNT mixtures and TATB, where observations indicate significant particle growth (50% or more) continues over several microseconds; however, our results converge with recent theoretical models[21].

VI. ACKNOWLEDGEMENTS:

This work was primarily funded by LLNL-LDRD (14-ERD-018) and performed under the auspices of the U.S. Department of Energy by Lawrence Livermore National Laboratory under Contract DE-AC52-07NA27344. The Dynamic Compression Sector at the Advanced Photon Source (DCS@APS) is managed by Washington State University and funded by the National Nuclear Security Administration of the U.S. Department of Energy under Cooperative Agreement DE-NA0002442. This research used resources of the Advanced Photon Source, a U.S. Department of Energy (DOE) Office of Science User Facility operated for the DOE Office of Science by Argonne National Laboratory under Contract No. DE-AC02-06CH11357. ChemMatCARS Sector 15 is supported by the National Science Foundation/Department of Energy under grant number NSF/CHE-1346572. The authors acknowledge experimental assistance by the DCS staff as well as useful discussions with G. Overturf, J. Maienschein, and J. Molitoris of LLNL as well as R. Gustavsen and D. Dattelbaum of LANL. LLNL-JRNL-666850.

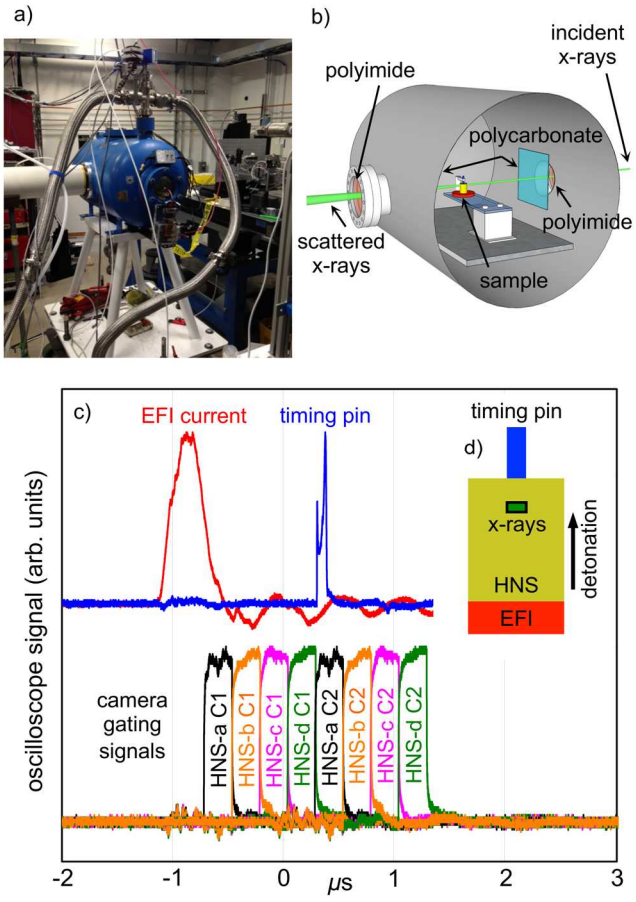

Figure 1: a) A photo of the detonation chamber. B) AThe experimental geometry with vacuum-containing polyimide windows, and polycarbonate blast/shrapnel shields, and sample position. c) Representative oscilloscope traces for the EFI current (red) and the piezo timing pin (blue) for shot HNS-a. The lower traces show camera gating temporal positions for C1 and C2 for four shots (HNS-a,b,c,d) relative to the EFI current and timing pin. d) A color coordinated schematic of sample geometry with the initiator at the bottom, detonation progressing from bottom to top, the timing pin, and approximate x-ray position 6.4 mm above the bottom surface of the HNS.

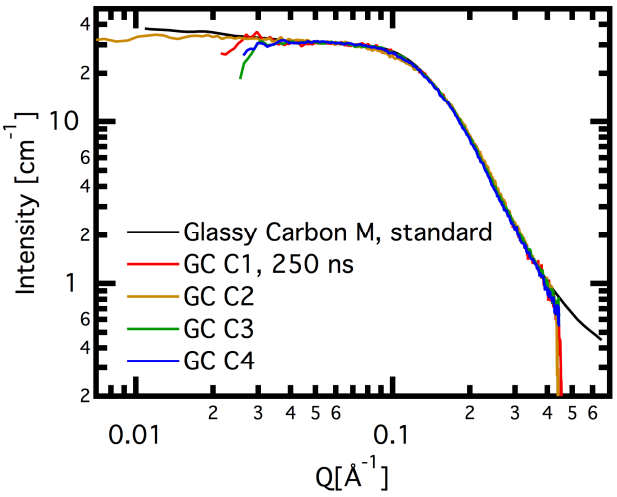

Figure 2: Glassy carbon M standard acquired at APS 15ID vs. acquisitions on the image-intensified 4-camera system; cameras designated C1-C4. Acquisitions acquired during APS 324-bunch mode, with 250 ns gating. The figure shows reliable SAXS at these intensities from $4x10^{-2}$ A^{-1} to $4x10^{-1}$ A^{-1}.

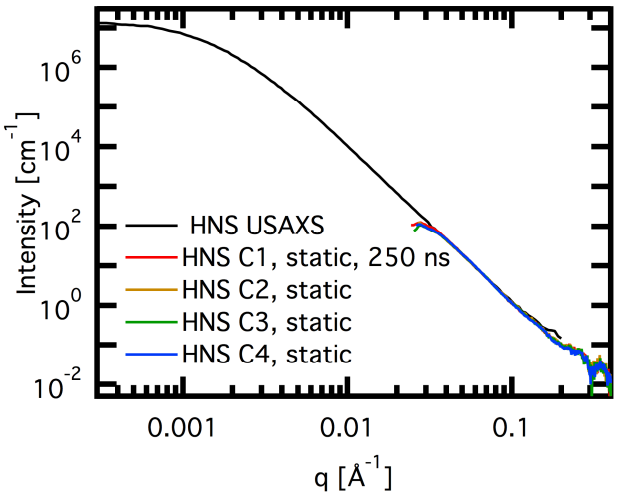

Figure 3: USAXS from pressed HNS acquired at APS 15ID vs. 2D SAXS acquired on the 4-camera system with 250 ns gating. Cameras are indicated C1-C4. The figure shows normalized SAXS is well-calibrated.

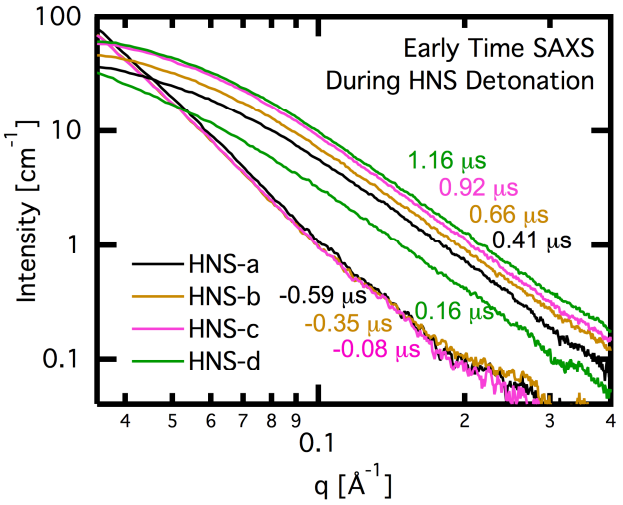

Figure 4: Small-angle X-ray scattering data with respect to the detonation front passing through the x-ray beam position. Traces are labeled by shot; here, we present the 1st two frames from shots a-d. For times less than 0, the scattering overlays scattering from undetonated HNS. In this figure, by 0.41 us, the SAXS shape stays constant while SAXS intensity rises through 1.16 us. The trace at 0.16 μs appears to be a superposition of undetonated HNS and post-detonation carbon condensates.

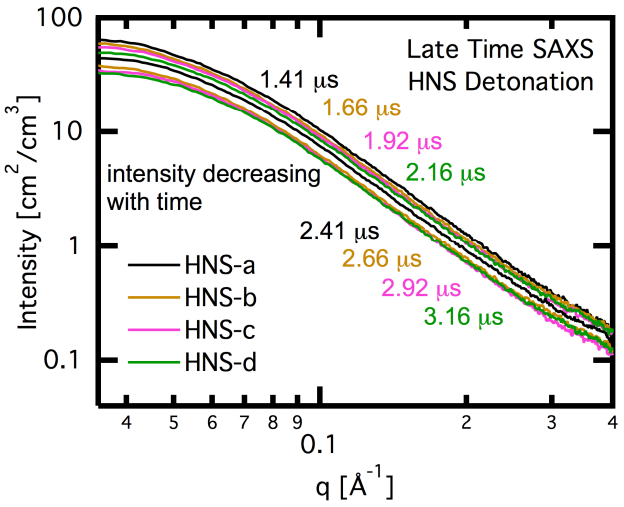

Figure 5: Small-angle X-ray scattering at later times compared with Fig. 4. The SAXS shape is constant while the intensity monotonically decreases from 1.41 to 3.16 microseconds.

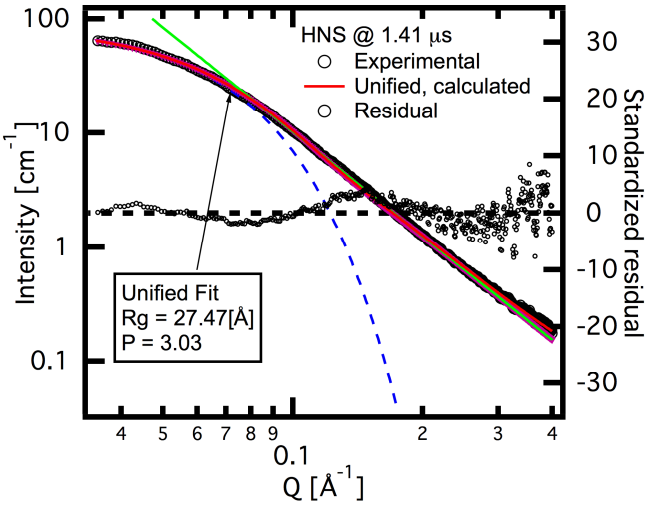

Figure 6: A representative unified fit for shot HNS-a, camera 3, at about 1.41 us after detonation. The black curve is data, the red is the total unified fit. Blue dashed and green represent Guinier and power-law components of the fit. Particularly the unified fits across shots from 0.41 to 3.16 μs show a power law slope of 3.0 +/- .1, and radius of gyration (Rg) of 27.5 +/- 0.6 Å.

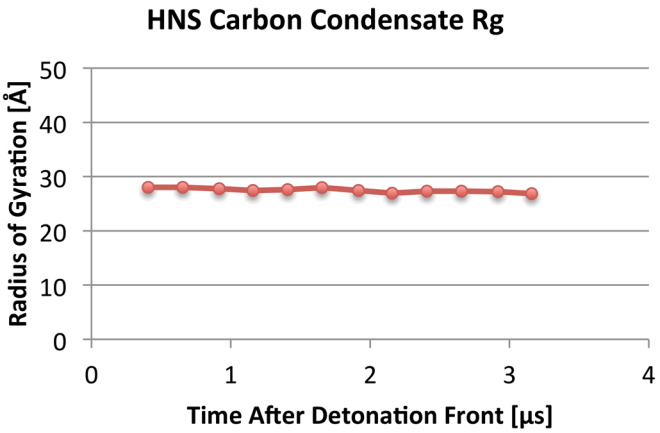

Figure 7: The Radius of Gyration (Rg) acquired by fitting the data from each shot with a single Guinier and Porod as seen in Fig. 6.

References

1. S. Bastea and L. E. Fried, in *Shock Wave Science and Technology Reference*, edited by F. Zhang (2012), Vol. 6.
2. S. Bastea and L. E. Fried, Proc. 14th Int. Det. Symp., 878 (2010).
3. N. Kubota, *Propellants and Explosives: Thermochemical Aspects of Combustion*. (Wiley-VHC, Germany, 2007).
4. S. Bastea, K. R. Glaesemann and L. E. Fried, Proc. 13th Int. Det. Symp., 1137 (2006).
5. I. B. Zeldovich and A. S. Kompaneets, *Theory of Detonation*. (Academic Press, New York, 1960).
6. C. M. Tarver, in *Shock Wave Science and Technology Reference*, edited by F. Zhang (2012), Vol. 6.
7. S. Bastea, Appl Phys Lett **100** (21) (2012).
8. J. A. Viecelli, S. Bastea, J. N. Glosli and F. H. Ree, J Chem Phys **115** (6), 2730-2736 (2001).
9. J. A. Viecelli and F. H. Ree, J Appl Phys **88** (2), 683-690 (2000).
10. J. A. Viecelli and F. H. Ree, J Appl Phys **86** (1), 237-248 (1999).
11. M. S. Shaw and J. D. Johnson, J Appl Phys **62** (5), 2080-2085 (1987).
12. M. R. Manaa, E. J. Reed, L. E. Fried and N. Goldman, J Am Chem Soc **131** (15), 5483-5487 (2009).
13. V. V. Danilenko, Phys. Solid State **46** (4), 595-599 (2004).
14. V. V. Danilenko, Combust Explo Shock+ **41** (5), 577-588 (2005).
15. N. R. Greiner, D. S. Phillips, J. D. Johnson and F. Volk, Nature **333** (6172), 440-442 (1988).
16. A. N. Aleshaev, P. I. Zubkov, G. N. Kulipanov, L. A. Luk'yanchikov, N. Z. Lyakhov, S. I. Mishnev, K. A. Ten, V. M. Titov, B. P. Tolochko, M. G. Fedotov and M. A. Sheromov, Combust Explo Shock+ **37** (5), 585-593 (2001).
17. E. R. Pruuel, K. A. Ten, B. P. Tolochko, L. A. Merzhievskii, L. A. Luk'yanchikov, V. M. Aul'chenko, V. V. Zhulanov, L. I. Shekhtman and V. M. Titov, Dokl Phys **58** (1), 24-28 (2013).
18. K. A. Ten, E. R. Pruuel and V. M. Titov, Fuller Nanotub Car N **20** (4-7), 587-593 (2012).
19. V. M. Titov, E. R. Pruuel, K. A. Ten, L. A. Luk'yanchikov, L. A. Merzhievskii, B. P. Tolochko, V. V. Zhulanov and L. I. Shekhtman, Combust Explo Shock+ **47** (6), 615-626 (2011).
20. O. Evdokov, M. G. Fedotov, G. N. Kulipanov, L. A. Luckjanchikov, N. Z. Lyakhov, S. I. Mishnev, M. R. Sharafutdinov, M. A. Sheromov, K. A. Ten, V. M. Titov, B. P. Tolochko and P. I. Zubkov, Nucl Instrum Meth A **470** (1-2), 236-239 (2001).
21. S. Bastea, presented at the Fifteenth International Detonation Symposium, San Francisco, CA, 2014 (unpublished).
22. C. M. Tarver and S. K. Chidester, 18th Aps-Sccm and 24th Airapt, Pts 1-19 **500**, 6 (2014).
23. B. J. Jensen, K. J. Ramos, A. J. Iverson, J. Bernier, C. A. Carlson, J. D. Yeager, K. Fezzaa and D. E. Hooks, 18th Aps-Sccm and 24th Airapt, Pts 1-19 **500**, 8 (2014).
24. Y. M. Gupta, S. J. Turneaure, K. Perkins, K. Zimmerman, N. Arganbright, G. Shen and P. Chow, Review of Scientific Instruments **83** (12), 10 (2012).
25. J. Ilavsky, J. Appl. Cryst. **45**, 324-328 (2012).
26. J. Ilavsky and P. R. Jemian, J. Appl. Cryst. **42** (42), 347-353 (2009).
27. F. Zhang, J. Ilavsky, G. G. Long, J. P. G. Quintana, A. J. Allen and P. R. Jemian, Metall Mater Trans A **41A** (5), 1151-1158 (2010).
28. B. Freelon, K. Suthar and J. Ilavsky, J. Appl. Cryst. **46**, 1508-1512 (2013).
29. J. Ilavsky, F. Zhang, A. J. Allen, L. E. Levine, P. R. Jemian and G. G. Long, Metall Mater Trans A **44A** (1), 68-76 (2013).
30. J. Ilavsky, A. J. Allen, L. E. Levine, F. Zhang, P. R. Jemian and G. G. Long, J. Appl. Cryst. **45**, 1318-1320 (2012).
31. G. Beaucage, J. Appl. Cryst. **28**, 717-728 (1995).
32. K. A. Ten, V. M. Titov, E. R. Pruuel, A. O. Kashkarov, B. P. Tolochko, Y. A. Aminov, B. G. Loboyko, A. K. Muzyrya and E. B. Smirnov, presented at the The 15th International Detonation Symposium, San Francisco, CA, 2014 (unpublished).
33. R.-J. Roe, *Methods of X-ray and Neutron Scattering in Polymer Science*. (Oxford University Press, New York, 2000).
34. T. Neugebauer, Ann Phys-Berlin **42** (7/8), 509-533 (1942).
35. O. Kratky and G. Porod, J Coll Sci Imp U Tok **4** (1), 35-70 (1949).